# Zero Poisson's Ratio Cellular Structure for Two-Dimensional Morphing Applications

Xiaobo Gong[1, 2], Jian Huang[2, 3], Fabrizio Scarpa[2], Yanju Liu[3] and Jinsong Leng[1]

[1]Centre for Composite Materials and Structures, Harbin Institute of Technology, Harbin HIT Science Park, No. 2 YiKuang Street, Harbin, 150080, PR China

Email: lengjs@hit.edu.cn

[2]Advanced Composites Centre for Innovation and Science, University of Bristol, Bristol BS8 1TR, UK

Email: f.scarpa@bristol.ac.uk

[3]Department of Astronautical Science and Mechanics, Harbin Institute of Technology P.O. Box 301, No. 92 West Dazhi Street, Harbin 150001, PR China

## ABSTRACT

This work presents a novel zero Poisson's ratio (ZPR) honeycomb structure that can achieve deformations along two orthogonal directions and avoid the increase of effective stiffness in the morphing direction by the restraining the Poisson's effect in the non-morphing direction. Opposite to current ZPR honeycombs for one-dimensional wing morphing the proposed novel zero Poisson's ratio honeycomb configuration can perform two-dimensional deformation and present a cellular structure with smooth edges. Analytical models related to the uniaxial, in-plane shear and bounds of the out-of-plane (transverse) shear stiffnesses are derived and validated using the finite element techniques. The in-plane behaviour of the honeycomb is investigated using a parametric analysis against the geometry of the unit cell, while the out-of-plane transverse stiffness is also evaluated versus the gauge thickness of the cellular honeycomb structure panels. The theoretical and numerical models exhibit good agreement and show the potential of this novel ZPR configuration for morphing sandwich panel cores.

**Keywords:** 2D morphing, zero Poisson's ratio, cellular structure, elastic constants

## 1 Introduction

Morphing aircraft can change their configurations in different points of their flight envelope to significantly improve the aerodynamic and aeromechanics performance and allows the aircraft to perform multiple missions. Morphing wing layouts are classified into three major types: planform alteration (involving span, chord, and sweep changes), out-of-plane transformation (twist, dihedral/gull, and span-wise bending), and airfoil adjustment (camber and thickness) [1, 2]. The morphing structure should possibly deform when subjected to low amplitude driving forces and withstand the aerodynamic load simultaneously [3], and therefore cannot be made by simply using conventional and readily available materials [4]. The morphing structure must also show a mechanical anisotropy with low in-plane stiffness to minimize the actuation energy, but also possess high out-of-plane stiffness to carry the aerodynamic pressure load. A cellular composite structure made from a honeycomb core with compliant face sheets has been proposed for morphing applications by Olympio and Gandhi [5], with low in-plane and high out-of-plane stiffness obtained when the honeycomb core has a sufficient transverse thickness without large weight penalties [6].

Cellular structures in general have attracted the attention of many engineers and technologists for several decades because of their lightweight and out-of-plane stiffness properties [7]. Several cellular structures with positive, negative and zero Poisson's ratio have been designed to satisfy different performance requirements. Conventional hexagonal honeycombs with positive Poisson's ratios have been widely used in the industry, and its elastic and nonlinear mechanical properties extensively investigated through theoretical analysis, finite elements methods and experiments [7-12]. When the cell geometry becomes re-entrant (i.e., butterfly shaped) the effective Poisson's ratio is transformed into negative [8, 13-17]. Besides the re-entrant honeycomb topology, there are some other auxetic cellular configurations such as the chiral [18-21], star-shaped [22], and double arrowhead honeycomb [23, 24]. These cellular configurations have however some drawbacks when used in morphing skins or morphing structures sections, because of the anticlastic or synclastic curvatures that positive and negative Poisson's ratio materials exhibit [9, 23], and these properties are not conducive to an efficient use in variable camber wing applications because of their out-of-plane deformation fields. On the other hand, when a conventional honeycomb is deformed along one direction, the large Poisson's contraction (or expansion in the case of auxetic honeycomb) occurs in the absence of any constraint in the non-morphing direction [25]. The Poisson's contraction or expansion can lead to a large increase in the 'effective' in-plane axial stiffness in the morphing direction, resulting in a corresponding increase of the required force for morphing actuation [25]. To overcome these shortcomings, zero Poisson's ratio (ZPR) honeycombs have been designed and fabricated [26-29], and characterized for morphing skins applications [6, 25, 30-32].

The majority of the current zero Poisson's ratio honeycomb configurations proposed in open literature are suitable for one-dimensional wing morphing only because they exhibit elongation along

only one direction while showing a non-uniform deformation along the transverse direction because of their sawtooth edges due to alternate contraction and expansion of the $+\theta/-\theta$ rows [25].

This work presents a novel zero Poisson's ratio honeycomb structure for two-dimensional morphing that can achieve the deformation along two orthogonal directions and at the same time avoid the effective substantial stiffness increase in the morphing direction by restraining the Poisson's deformation in the non-morphing direction. The elasticity of this ZPR honeycomb is investigated using theoretical and numerical techniques. The in-plane uniaxial and shear engineering constants have been derived with an analytical model and validated by a finite element analysis. The out-of-plane properties and the transverse shear modulus, were characterised through numerical interpolation formulas relating analytical upper and lower (Reuss and Voigt) shear modulus bounds.

## 2 The zero Poisson's ratio honeycomb design

The layout of the novel zero Poisson's ratio honeycomb and its unit cell are presented in Figure 1. The unit cell possesses a horizontal, vertical and central symmetry. The geometry of unit cell can be expressed by defining two walls with lengths H and L, thickness t, and two internal cell angles (φ and θ). The gauge thickness of the honeycomb structure panels is indicated as b. As other notations used in the Cellular Material Theory [7], the geometry of the unit cell is also defined by nondimensional parameters like α, β, and γ (cell wall aspect ratio $\alpha = H/L$, thickness ratio $\beta = t/L$, gauge thickness ratio $\gamma = b/L$).

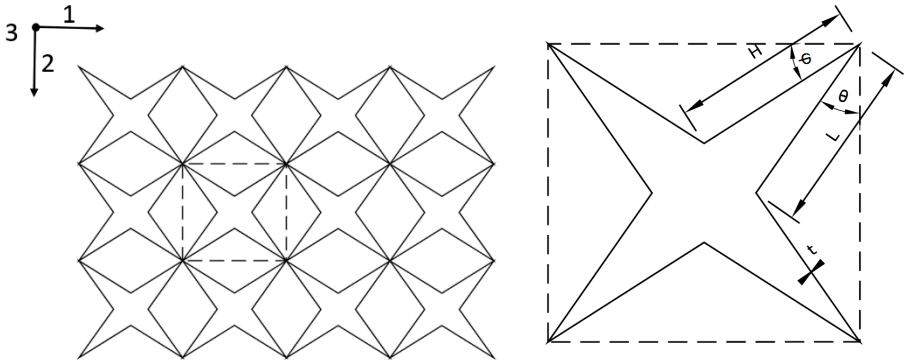


Figure 1 Layout of the novel zero Poisson's ratio honeycomb and geometric parameters of a unit cell.

The geometric parameters of the unit cell needs to satisfy the following constraints and inequalities to avoid contacts and intersections of the walls:

$$\theta > 0 \quad (1)$$
$$\varphi > 0 \quad (2)$$
$$\theta < \frac{\pi}{2} - \varphi \quad (3)$$
$$cos\theta > \alpha sin\varphi \quad (4)$$
$$sin\theta < \alpha cos\varphi \quad (5)$$

Solving the above inequalities, one can obtain a map of the admissible intervals of the angles φ and θ under different aspect ratios α. When $\alpha < 1$, we obtain:

$$0 < \varphi < \frac{\pi}{2} \tag{6}$$

$$0 < \theta < \arcsin(\alpha cos\varphi) \tag{7}$$

Conversely, when $\alpha \geq 1$, the range of the parameters are the following:

$$0 < \varphi < \arcsin\left(\frac{1}{\alpha}\right) \tag{8}$$

$$0 < \theta < \arccos(\alpha sin\varphi) \tag{9}$$

Figure 2 shows the feasible ranges of the angles θ and φ with different aspect ratios α. The widest feasible range of geometry parameters occurs when $\alpha = 1$. The more the aspect ratio deviates from 1, the narrower the admissible range of the internal cell angles become. Because of the unit cell symmetry, the curves corresponding to $\alpha = 0.5$ and $\alpha = 2$ are symmetric about the line φ=θ. The symmetry means that the mathematical functions describing these curves are mutually inverse, and the angles θ and φ have similar admissible ranges at the corresponding aspect ratio.

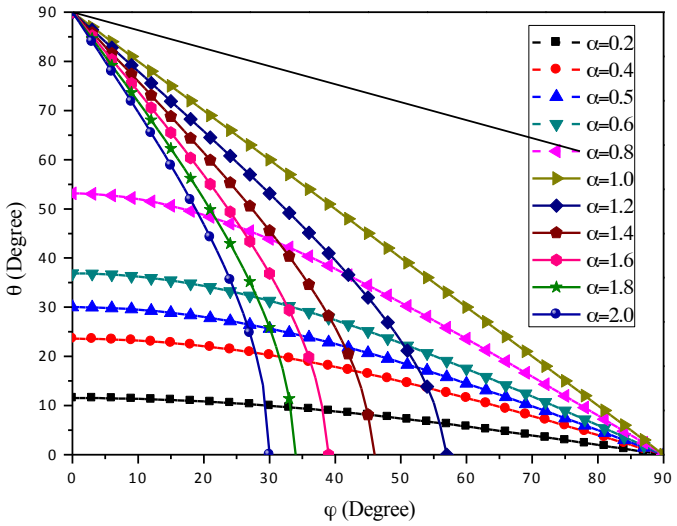


Figure 2 Feasible ranges of angles θ and φ with different aspect ratio α.

The relative density is an important parameter for a honeycomb structures, and it is defined by:

$$\frac{\rho}{\rho_s} = \frac{A}{A_s} \tag{10}$$

In (10), $A$ and $A_s$ are respectively the cross-sections perpendicular to the honeycomb thickness direction and the load bearing area. Here, we assume that the honeycomb has low β values [7], and

that all cell walls have the same thickness. The cross-section area can be calculated by multiplying the total cell wall length and wall thickness, and the relative density of the honeycomb results in:

$$\frac{\rho}{\rho_s} = \frac{\beta(\alpha+1)}{\alpha cos\theta cos\varphi} \tag{11}$$

## 3 Analytical model

### 3.1 In-plane mechanical properties of the zero Poisson's ratio honeycomb

The theoretical analysis that describes the in-plane mechanical properties is based on the use of Castigliano's second theorem. The analytical model is based on the assumption that the cell wall undergoes axial and flexural deformations. When a stress σ is applied on the horizontal direction (1), one set of cell walls along the 1-direction carries the load. By symmetry, the quarter unit cell is considered with two fixed-ends and loaded along the 1-direction (Figure 3).

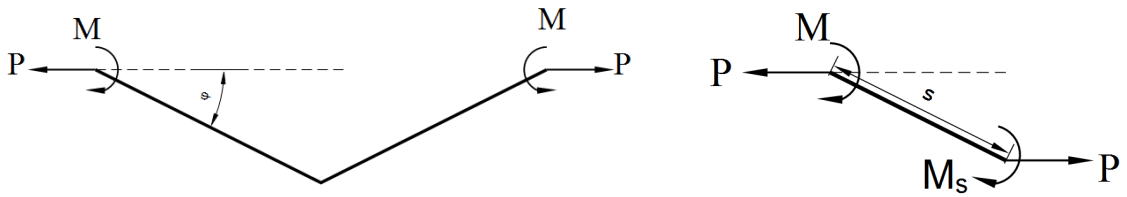


(a) (b)

Figure 3 Forces and moments corresponding to the homogenized horizontal (1) direction tensile properties: (a) fixed-ends of quarter unit cell, (b) arbitrary section of the beam.

From the equilibrium of the moments on the left end of the beam, the distribution of moments at an arbitrary section can be obtained as:

$$M_s = P \cdot s \cdot sin\varphi - M \tag{12}$$

In which:

$$P = \sigma L b cos\theta \tag{13}$$

The deflection angle can be obtained by integrating the bending-moment equation:

$$\Delta(s) = \int \frac{M_s}{E_s I} ds + c \tag{14}$$

In (14), $c$ is a constant of integration, $E_s$ is the young's modulus of the initial material, and $I$ is second moment of area of the beam. For symmetry, the deflection angle at the turning point of the cell wall is zero, therefore we have the boundary conditions $\Delta(0) = 0, \Delta(\mathrm{H}) = 0$. Applying these BCs to Eq. (14) we obtain:

$$c = 0 \tag{15}$$

$$M = \frac{PHsin\varphi}{2} \tag{16}$$

The displacement along the 1-direction can be obtained by the unit-load equation for the case where axial and flexural deformations are considered:

$$\delta = \int \frac{M_S M_1}{E_S I} ds + \int \frac{F_S F_1}{E_S A} ds \tag{17}$$

In which $M_s$ and $F_s$ are actual loads, and $M_1$ and $F_1$ are unit loads (moments and forces). The formulation of the actual loads are:

$$M_S = Pssin\varphi - \frac{PHsin\varphi}{2} \tag{18}$$
$$M_1 = ssin\varphi - \frac{Hsin\varphi}{2} \tag{19}$$
$$F_S = Pcos\varphi \tag{20}$$
$$F_1 = cos\varphi \tag{21}$$

By substituting the expressions $M_S$, $M_1$, $F_S$ and $F_1$ into equation (17) we obtain:

$$\delta = \frac{P\alpha^3 L^3 sin\varphi^2}{12E_S I} + \frac{P\alpha L cos\varphi^2}{E_S A} \tag{22}$$

The strain along the 1-direction is expressed as:

$$\varepsilon = \frac{\delta}{\alpha L cos\varphi} \tag{23}$$

The Young's modulus along the 1-direction is formulated as follows:

$$E_1 = \frac{\sigma}{\varepsilon} \tag{24}$$

Substituting the expressions $\sigma$ and $\varepsilon$ in (24) we obtain the expression of the nondimensional Young's modulus along the direction 1:

$$\frac{E_1}{E_S} = \frac{\beta^3 cos\varphi}{cos\theta(\alpha^2 sin\varphi^2 + \beta^2 cos\varphi^2)} \tag{25}$$

Due to the symmetry, the rotation at the intersection of the walls with different lengths is assumed to be zero. By ignoring the deformation at the point of intersection, the inclined walls along the 1 direction (with length H) and in the 2-direction (with length L) have independent deformations. The deformations of the cell walls along the 1-direction with the length H are only dependent on the H and $\varphi$ parameters. Meanwhile, the deformations of the cell walls along the 2-direction (length L) remain zero during loading along the 1-direction, and the strain along the 2-direction is zero. As a result, the Poisson's ratio $\upsilon_{21}$ is zero.

A similar methodology can be used to obtain the Young's modulus along the 2-direction, and the resulting nondimensional modulus is:

$$\frac{E_2}{E_s} = \frac{\beta^3 cos\theta}{\alpha cos\varphi(sin\theta^2+\beta^2 cos\theta^2)} \tag{26}$$

Similar consideration made above for the $\nu_{21}$ Poison's ratio can be applied when a tensile loading is exerted on the 2-direction, and the Poisson's ratio $\nu_{12}$ is also zero.

When comparing equations (25) and (26) it is possible to observe that the expression of $E_2$ can be obtained from the formulation of $E_1$ by swapping the geometric parameters (H with L, and $\theta$ with $\varphi$). The transformations can also be expressed by replacing $1/\alpha$ with $\alpha$, and $\beta/\alpha$ with $\beta$. The symmetry of the lattice allows these transformations, which simplify the modeling of the honeycomb configuration.

To calculate the homogenized shear modulus a uniform shear stress is applied to the honeycomb, as shown in Figure 4. The honeycomb undergoes pure shear in an antisymmetric system, due to the symmetry of the geometry but the antisymmetric loading present in this configuration. A quarter unit cell is isolated by cutting along the horizontal and vertical symmetry planes. Antisymmetric systems have only antisymmetric internal forces at symmetric planes, therefore only antisymmetric shear load ($F_1$ and $F_2$) at the symmetric cross sections are present.

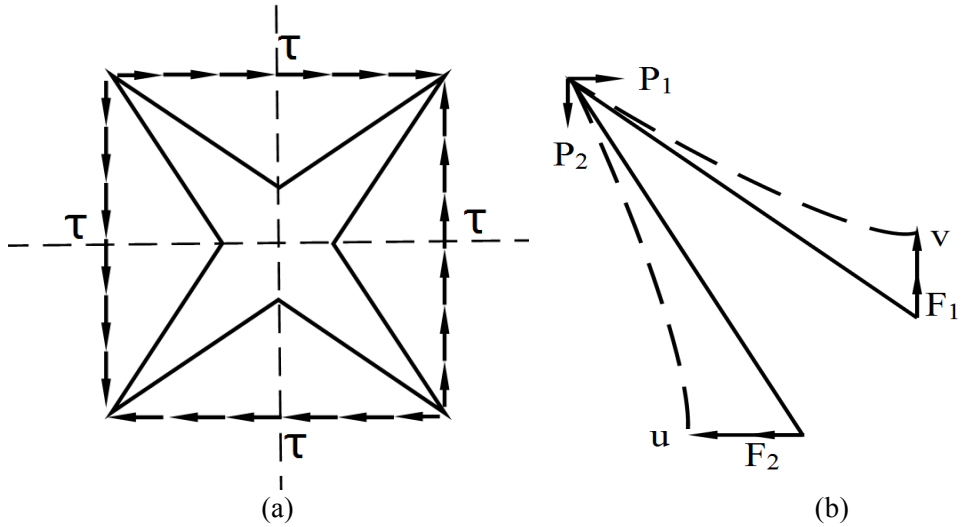


Figure 4 The honeycomb in pure shear: (a) unit cell subjected to pure shear stress; (b) the loads and displacements of the quarter unit cell caused by a shear stress.

The loads can be determined from the equilibrium of the quarter unit cell ($F1=P_2$; $F_2=P_1$), for which:

$$P_1 = \tau\alpha L cos\varphi \quad (27)$$
$$P_2 = \tau L cos\theta \quad (28)$$

By using standard beam theory for cantilever beams [33], the deflection can be calculated as $\omega = (Fl^3)/3EI$. The shearing deflections $u$ and $v$ corresponding to the horizontal and vertical directions are derived as:

$$v = \frac{F_1 cos\varphi(\alpha L)^3 cos\varphi}{3E_s I} \quad (29)$$
$$u = \frac{F_2 cos\theta L^3 cos\theta}{3E_s I} \quad (30)$$

The shear strain $\gamma_{12}$ is therefore obtained as:

$$\gamma_{12} = \frac{v}{\alpha L cos\varphi} + \frac{u}{L cos\theta} \quad (31)$$

The shear modulus is $G_{12} = \tau/\gamma_{12}$, and the related nondimension in-plane shear modulus is finally expressed as:

$$\frac{G_{12}}{E_s} = \frac{\beta^3}{4(\alpha^2+\alpha)cos\theta cos\varphi} \quad (32)$$

### 3.2 Out-of-plane mechanical properties

The out-of-plane mechanical properties of the zero Poisson's ratio honeycomb are described by the transverse Young's modulus $E_3$ for the normal loading along the gauge thickness direction (3), and the transverse shear moduli $G_{13}$ (and $G_{23}$). The transverse modulus $E_3$ scales as the relative density [7]:

$$\frac{E_3}{E_s} = \frac{\beta(\alpha+1)}{a cos\theta cos\varphi} \quad (33)$$

The expressions related to the transverse shear moduli are more complicated, due to the absence of a simple stress distribution. Each cell face bears a non-uniform deformation and does not remain plane because of the constrains imposed [7]. Exact calculations are only possible by using numerical methods [11, 16, 21, 34, 35]. However, the upper and lower bounds (Voigt and Reuss) of the two transverse shear moduli can be calculated by using a simplification of the method proposed by Kelsey et al [7, 36]. The two bounds involve the calculation of the strain energy associated with a strain distribution that allows compatible deformations, and the application of a stress distribution that satisfies equilibrium.

Let us consider a uniform shear strain $\gamma_{13}$, caused by a shear stress $\tau_{13}$ applied along the 1-direction to the face normal to the 3-axis. Almost all the elastic strain energy of the honeycomb cell

can be considered dissipated with the shear deformation of the cell walls, the bending stiffness and the energies associated with bending being significantly smaller [7]. The theorem of minimum potential energy can be therefore written as an inequality for the shear along the 1-direction:

$$\frac{1}{2}G_{13}{\gamma_{13}}^2V \leq \frac{1}{2}G_s\sum({\gamma_{1i}}^2V_i) \tag{34}$$

In (34), $G_s$ is the shear modulus of the cell wall material, $\gamma_{1i}$ are the shear strains in the cell wall and the summation is carried over the cell walls with volumes $V_H$ and $V_L$.

The transverse shear strains in the cell walls with lengths H and L are:

$$\gamma_H = \gamma_{13}cos\varphi \tag{35}$$

$$\gamma_L = \gamma_{13}sin\theta \tag{36}$$

By evaluating the sum one obtains:

$$\frac{G_{13}}{G_s} \leq \frac{\beta(\alpha cos\varphi^2+sin\theta^2)}{\alpha cos\theta cos\varphi} \tag{37}$$

The theorem of minimum complementary energy provides the lower bound for the transverse shear modulus. When shear along the 1-direction is applied, the theorem can be expressed as an inequality:

$$\frac{1}{2}\frac{{\tau_{13}}^2}{G_{13}}V \leq \frac{1}{2}\frac{1}{G_s}\sum({\tau_i}^2V_i) \tag{38}$$

The global shear stress $\tau_{13}$ on the face normal to the 3-axis along the 1-direction induce the local shear stresses $\tau_H$ and $\tau_L$. By symmetry, the equilibrium along the 2 and 3 directions can be obtained automatically. The resultant external shear stress along the 1-direction therefore is:

$$\tau_{13}Hcos\varphi Lcos\theta = \tau_H tHcos\varphi + \tau_L tLsin\theta \tag{39}$$

Equations (38) and (39) are not directly solvable, and the lower bounds do not have a closed form solution but need to be obtained using numerical techniques like the finite element approach [21, 34]. The transverse shear modulus has an inverse correlation with the gauge thickness ratio $\gamma$, due to the effect of the in-plane bending deformations of the walls [11, 16, 21, 34, 35]. The transverse shear modulus remains almost constant for a gauge thickness ratio $\gamma$ higher than 20 [34]. In this work, the lower bound of this new zero Poisson's ratio honeycomb is identified for a ratio $\gamma$ of 30 by Finite Element simulations (for details please see paragraph 4). Like in the case of hexagonal

centrosymmetric honeycombs, the transverse shear modulus can be calculated by interpolating the upper ($G_U$) and lower ($G_L$) shear moduli bounds as a function of the gauge thickness ratio [11, 34]:

$$G_{13} = G_L + f(\gamma)(G_U - G_L) \tag{40}$$

A least-squares fitting ($R^2$=0.98 and 95% confidence level) over 1146 configurations of the zero Poisson's ratio honeycomb gives a reasonable approximation of the transverse shear modulus. In the 13 plane. Quite differently from the hexagonal honeycomb for which $f(\gamma) = K/\gamma$, the function $f(\gamma)$ has a more complex relation:

$$f(\gamma) = \alpha\gamma^b + c \tag{41}$$

In (40) *a*=1.4052, *b*=-0.50285 and *c*=-0.30149.

**4 Finite element modelling**

To validate the in-plane and out-of-plane linear elastic properties of the honeycomb structures numerical simulation have been performed using a commercial FE analysis package (ANSYS, version 15.0, Ansys Inc.). The elements used in the models have a constant thickness and linear elastic and isotropic material properties. Full-scale models consisting of 10 X 50 unit cells for the estimation of the Young's modulis and 10 X 10 unit cells for the in-plane shear modulus and the transverse modulus have been developed,(Figure 5). After a convergence test the mesh density was fixed at 10 elements per length *l*. The cell geometric configurations considered in the simulations were three aspect ratio values $\alpha$ (0.5, 1.0 and 2.0) constant cell wall thickness ratio $\beta = 0.1$ and angles θ and φ ranging between 5° and 80° with a step 5°. The material properties were set as the ABSplus basic material used in the fused deposition modelling (FDM) systems [27] ( $E_s = 2.265$GPa and Poisson's ratio $\upsilon_s = 0.25$).

The 2D FE models representing the in-plane mechanical properties were developed by using BEAM189 elements with three nodes and six degrees of freedom (including translations in the x, y, and z directions, and rotations about the 3 Cartesian axis). The tensile and shear deformations of the honeycomb under a linear static loading were developed by imposing rotations and displacements along the 1 and 2 directions in all nodes on lines A and B in Figure 5(a). The boundary conditions are listed in Table 1. All degrees of freedom of the nodes on line B were coupled. For the shear deformation the nodes belonging to lines C and D had antisymmetric boundary conditions to produce a state of pure shear. The homogenised stresses were calculated by averaging the reaction forces along the direction of the imposed displacements over the honeycomb boundary (line B). The average tensile and shear strains were calculated as the ratios between the imposed displacements. The moduli $E_1$ and $G_{12}$ were then obtained as the ratios between the averaged stresses and the imposed strains.

For the out-of-plane properties, the 3D FE models were developed by using SHELL181 elements with different geometric configurations. The SHELL181 element has four nodes and six degrees of freedom at each node (including translations in x, y, and z directions and related rotations. The transverse shear deformations of the honeycomb were created by imposing rotations and displacements along the 1 and 2 directions for all the nodes belonging to the surfaces E and F (Figure 5(b)). The boundary conditions are also listed in Table 1. The nodes on surfaces A and B had antisymmetric boundaries, while the nodes placed on surfaces C and D had symmetric boundary conditions to avoid the effects of the free boundaries. The homogenised stresses were calculated by averaging the reaction forces along the direction of the imposed displacements over the honeycomb boundary (surface F). The average transverse shear strains were calculated as the ratios between the imposed displacements ($u_1$) and gauge thickness. Finally, the modulus $G_{13}$ were obtained as ratios between the averaged stresses and imposed strains.

Table 1 Boundary conditions on the FE models to calculate the engineering constants

| Boundary | In-plane properties | Out-of-plane properties | |
|---|---|---|---|
| | $E_1$ | $G_{12}$ | $G_{13}$ |
| A | $u_1 = u_2 = u_3 = 0$ | $u_1 = u_2 = u_3 = 0$ | Antisymmetric |
| B | $u_1 = imposed, u_2 = u_3 = 0$ | $u_2 = imposed, u_3 = 0$ | Antisymmetric |
| C | Free | Antisymmetric | Symmetric |
| D | Free | Antisymmetric | Symmetric |
| E | | | $u_1 = u_2 = u_3 = 0$<br>$rot_1 = rot_2 = rot_3 = 0$ |
| F | | | $u_1 = imposed, u_2 = u_3 = 0$<br>$rot_1 = rot_2 = rot_3 = 0$ |

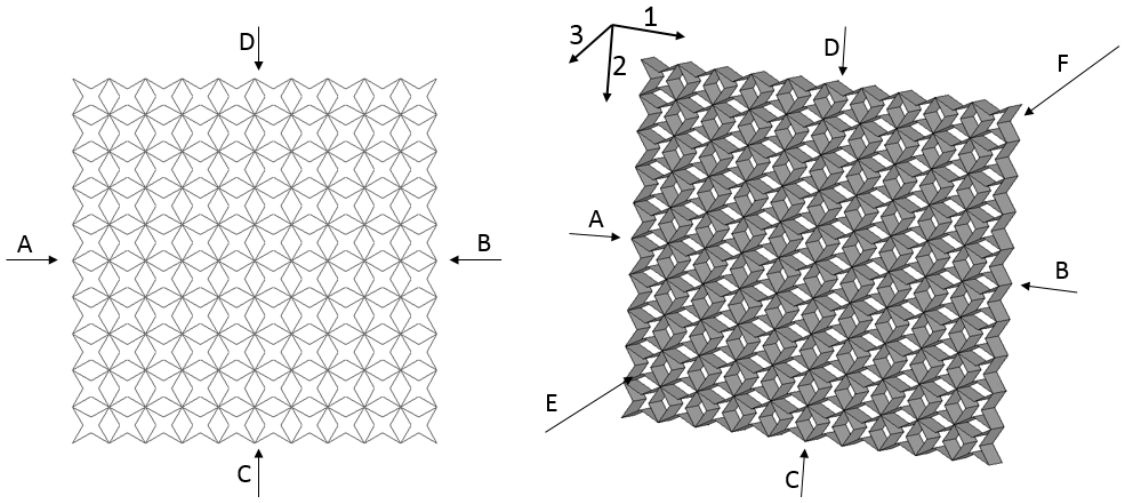


(a) (b)

Figure 5 Finite element models: (a) 2D geometric model for the simulation of the in-plane properties, (b) 3D geometric model for the out-of-plane properties.

**5 Results and discussions**

Figures 6-8 show the comparison between the FE homogenization and the theoretical predictions for the non-dimensional Young's modulus $E_1/E_s$ versus $\varphi$ and $\theta$ for $\beta = 0.1, \gamma = 1, \alpha = 0.5,\ 1.0,\ 2.0$. The feasible ranges of the angles θ and φ are calculated according to the geometrical limits (Figure 2). The nondimensional Young's modulus decreases with increasing value of the angle $\varphi$, but decreases for increasing values of $\alpha$ and the angles $\theta$. Cell walls of length H tend to increase the bending deformation for increasing length (corresponding to increasing $\alpha$ values) and increasing inclined angles $\varphi$. The bending deformations result in larger effective strains, and therefore lead to lower effective Young's modulus. The angle $\theta$ and the length L determine the effective load along the 1-direction by changing the section area perpendicular to the loading direction. The section area decreases with increasing angles $\theta$, and as a result the Young's modulus tends to decrease accordingly. Young's modulus values obtained by using the finite element techniques show a very close agreement with the theoretical predictions, although they tend to be more conservative compared to the analytical results The main sources of discrepancy come from the different models used in the FE homogenization and theoretical analysis. The FEM beam model used is based on Timoshenko beam theory, while the beam model used in theoretical analysis is an Euler-Bernoulli beam. By ignoring the transverse shear strains the theoretical analysis gives a smaller effective deformation that results in a higher Young's modulus. The relative errors increase with the angle $\varphi$ and decrease with the aspect ratio $\alpha$ (the largest errors are 10.4%, 3.4%, and 1.0% for $\alpha = 0.5, 1.0, 2.0$.).

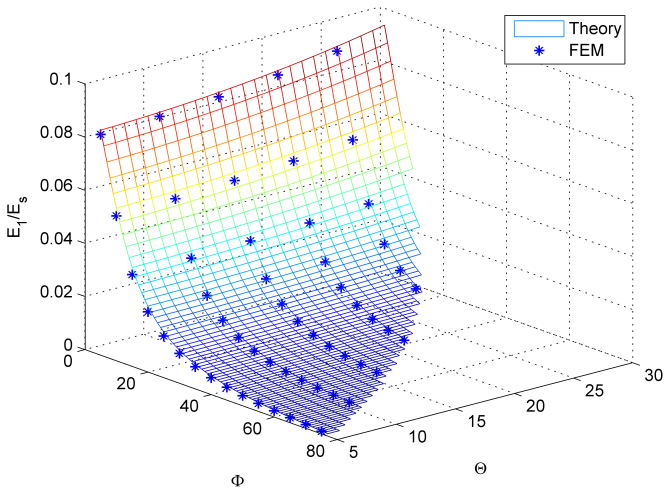


Figure 6 FE homogenization and theoretical predictions for the non-dimensional Young's modulus $E_1/E_s$ versus $\varphi$ and $\theta$ for $\beta = 0.1, \gamma = 1, \alpha = 0$..

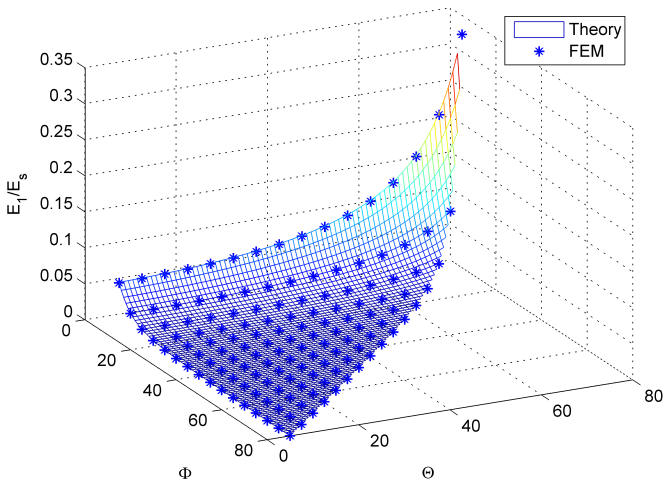


Figure 7 FE homogenization and theoretical predictions for the non-dimensional Young's modulus $E_1/E_s$ versus $\varphi$ and $\theta$ for $\beta = 0.1, \gamma = 1, \alpha = 1.0$.

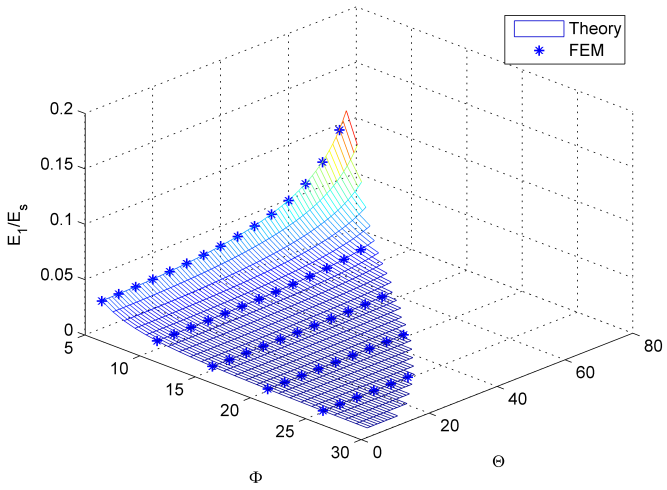


Figure 8 FE homogenization and theoretical predictions for the non-dimensional Young's modulus $E_1/E_s$ versus $\varphi$ and $\theta$ for $\beta = 0.1, \gamma = 1, \alpha = 2.0$.

Figure 9 shows the results of the FE homogenization for the Poisson's ratio $\upsilon_{21}$ versus $\varphi$ and $\theta$ for $\beta = 0.1, \gamma = 1, \alpha = 0.5$, 1.0, 2.0. Within the theoretical analysis it is assumed that the inclined walls along the 1-direction (with length H) and along the 2-direction (with length L) have independent deformations due to the symmetry, and therefore the Poisson's ratio $\upsilon_{21}$ is zero. This assumption was validated in a substantial way by the FEM results. The largest value of the Poisson's ratio $\upsilon_{21}$ is $4.1\text{X}10^{-4}$ which occurs at $\alpha = 1.0, \varphi = 5°, \theta = 75°$. The largest value drops to $1.1\text{X}10^{-4}$ when the feasible ranges of the angles θ and φ are limited to 5° and 40°. The average value of all the numerical simulations data shown in the figure is $3.5\text{X}10^{-5}$, which is a very small value, and significantly lower than the intrinsic Poisson's ratio of the core material. The novel honeycomb configuration proposed can be therefore effectively considered as a ZPR lattice with the ability of deforming in two dimensions. According to Olympio and Gandhi [25], the zero Poisson's ratio effect can avoid a substantial increase of the effective stiffness in the morphing direction by restraining the Poisson's contraction (or bulging) in the non-morphing direction. The existence of a lattice with the two in-plane Poisson's ratio equal to zero means means that the honeycomb is suited for two-dimensional morphing applications.

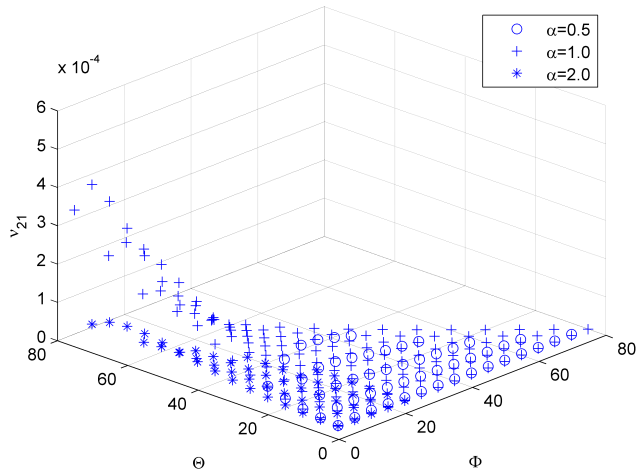


Figure 9 FE homogenization for the Poisson's ratio $\vartheta_{21}$ vs $\varphi$ and $\theta$ for $\beta = 0.1, \gamma = 1, \alpha = 0.5$, 1.0, 2.0.

Figures 10 to12 show the comparison between the FE homogenization and the theoretical predictions for the non-dimensional elastic modulus $G_{12}/E_s$ versus $\varphi$ and $\theta$ for $\beta = 0.1, \gamma = 1, \alpha = 0.5, 1.0, 2.0$. The in-plane shear modulus increases with increasing angles $\varphi$ and $\theta$, while decreases also in this case with increasing $\alpha$ values. The more compact the cell units are, the larger the in-plane shear modulus becomes. In contrast with the Young's modulus, the largest in-plane shear modulus values occur at $\varphi = 80°, \theta = 5°$ for $\alpha = 0.5$ . Similarly to the case of the Young's modulus, the shear modulus obtained by the finite element simulations show a close agreement with the theoretical predictions, with a largest relative error 5.7% occurring at $\alpha = 0.5, \varphi = 5° \; and \; \theta = 75°$, while the average relative error is around 1.5%. Also in this case, the results from the FE calculations are somehow more conservative than the analytical ones. The main sources of discrepancy also come from the different beam models used in the FE homogenization and in the theoretical analysis.

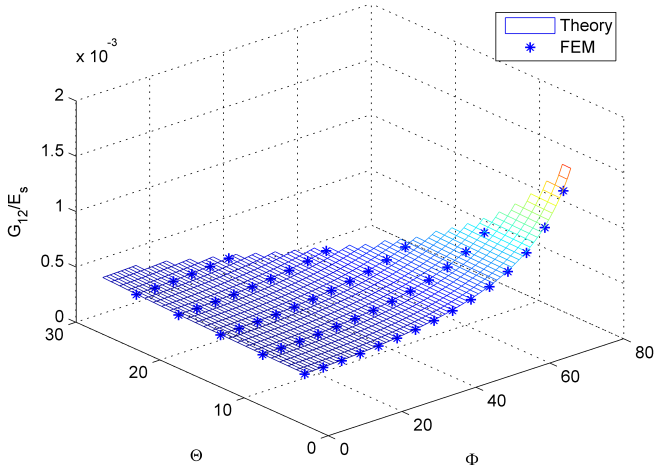


Figure 10 FE homogenization and theoretical predictions for the non-dimensional elastic modulus $G_{12}/E_s$ versus $\varphi$ and $\theta$ for $\beta = 0.1, \gamma = 1, \alpha = 0.5$.

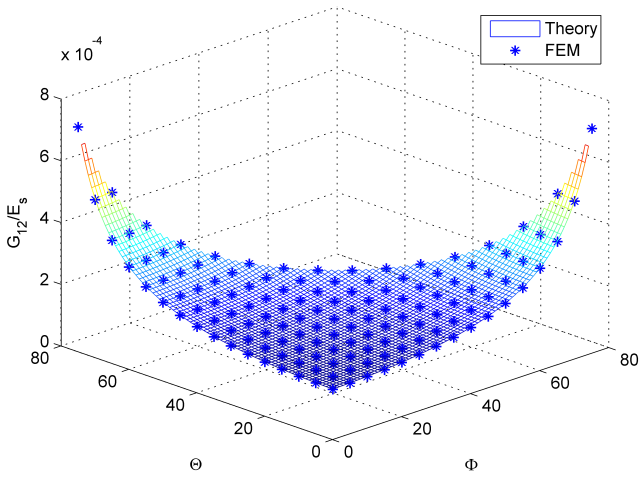


Figure 11 FE homogenization and theoretical predictions for the non-dimensional elastic modulus $G_{12}/E_s$ vs $\varphi$ and $\theta$ for $\beta = 0.1, \gamma = 1, \alpha = 1.0$.

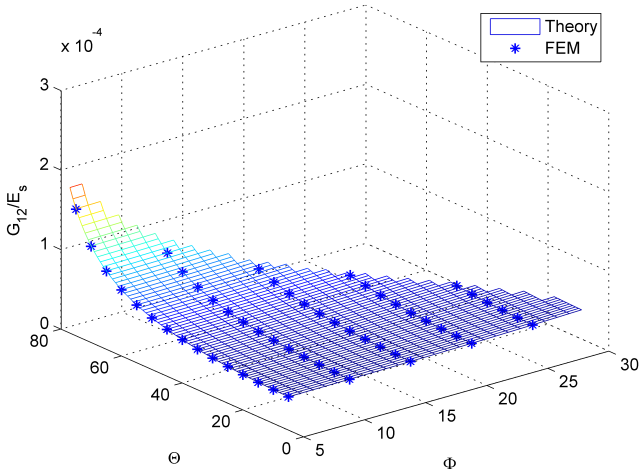


Figure 12 FE homogenization and theoretical predictions for the non-dimensional elastic modulus $G_{12}/E_s$ vs $\varphi$ and $\theta$ for $\beta = 0.1, \gamma = 1, \alpha = 2.0$.

Figure 13 shows the non-dimensional transverse Young's modulus $E_3/E_s$, which can be the density ratio $\rho/\rho_s$. The same with the in-plane shear modulus, when thickness ratio β is kept constant, the non-dimensional transverse Young's modulus increases with the increasing angle $\varphi$ and $\theta$, while decreases with the increasing $\alpha$.

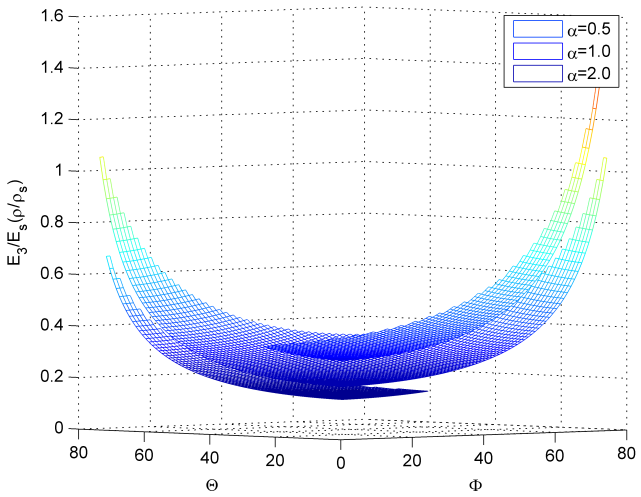


Figure 13 Theoretical results for relative density versus $\varphi$ and $\theta$ for $\beta = 0.1, \gamma = 1, \alpha = 0.5,1.0,2.0$.

Figures 14-17 show the results related to the theoretical upper bound and the numerical lower bound of the non-dimensional transverse shear modulus versus $\varphi$ and $\theta$ for $\beta = 0.1, \gamma = 1, \alpha = 0.5, 1.0, 2.0$. Similarly to what observed firstly by Grediac and then other Authors [11, 16, 21, 34, 35], the transverse shear modulus has an inverse relation with the gauge thickness ratio $\gamma$ due to the effect of the wall in-plane bending deformation. Figure 14 also shows the non-dimensional transverse shear modulus versus the internal cell angles for different γ values (γ=1, γ=20.) and β=0.1, α=1.0. In this work, the lower bound of this ZPR honeycomb is identified for a ratio $\gamma$ of 30. Figures 15-17 illustrate the theoretical upper bound and the numerical lower bound of the non-dimensional transverse shear modulus again versus the internal cell angles, this time for the series of parameters β=0.1, γ=1 and α=0.5, 1.0, 2.0. The upper and lower bounds increase as the angle θ increase, but diminish with increasing α and φ values. The difference between the upper and lower bound increases as the angle φ and θ increase, and tend to decrease for larger α parameters. The values of the bounds appear to be more sensitive to the angle θ. Unlike the hexagonal honeycomb case, the cell walls transverse to the 2-direction (with length L) are not vertical, but inclined at an angle θ. The wall with length L will therefore withstand a combination of shear and bending deformations, resulting in a non-unique value of the shear modulus, and therefore giving rise to upper and lower bounds. The shear deformation in the cell walls will be dominant for small φ or large θ angles when subjected to a transverse shear stress along the 1-direction.

As in the case of hexagonal centrosymmetric honeycombs, the transverse shear modulus can be approximated by linking through the gauge thickness the upper ($G_U$) and lower ($G_L$) shear bounds. The relation can be expressed as in equation (41), which is obtained by a least-squares fitting ($R^2$=0.98 and 95% confidence level) over 1146 configurations. Figure 18 show the non-dimensional

transverse shear modulus $G_{13}/G_S$ vs. γ for $\alpha = 1, \varphi = \theta = 30°, \beta = 0.1$. A significant agreement between the FEM data and approximated relation can be observed.

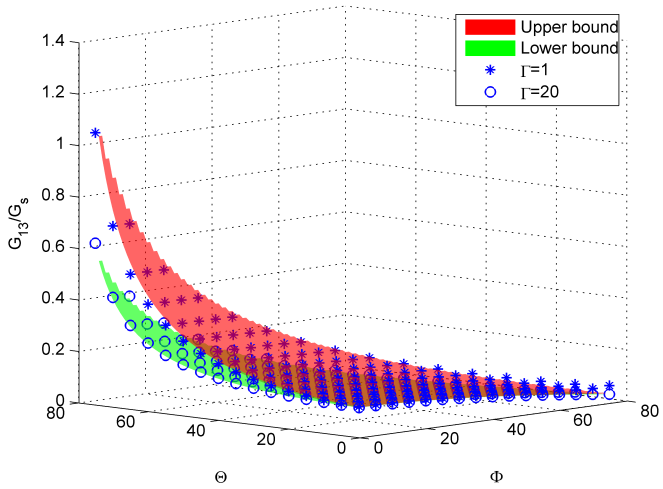


Figure 14 Non-dimensional transverse shear modulus vs. $\varphi$ and $\theta$ for different γ ($\gamma = 1, \gamma = 20.$) and $\beta = 0.1, , \alpha = 1.0$.

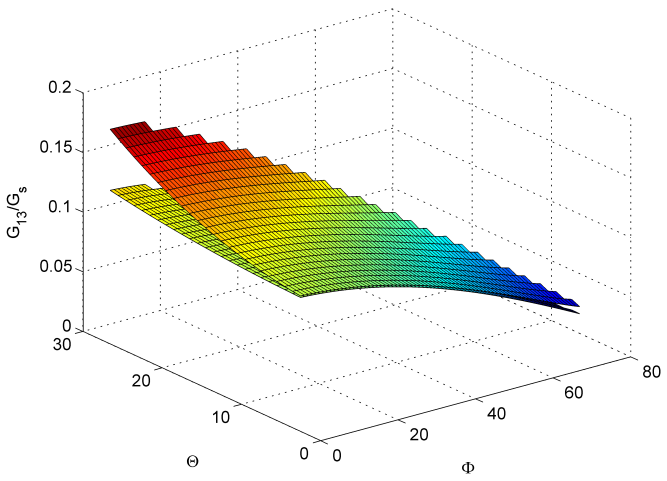


Figure 15 Theoretical upper bound and numerical lower bound of the non-dimensional transverse shear modulus vs. $\varphi$ and $\theta$ for $\beta = 0.1, \gamma = 1, \alpha = 0.5$.

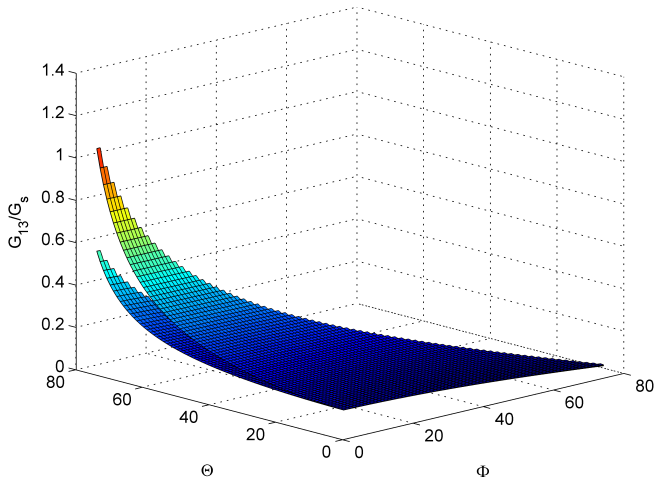


Figure 16 Theoretical upper bound and numerical lower bound of the non-dimensional transverse shear modulus vs. $\varphi$ and $\theta$ for $\beta = 0.1, \gamma = 1, \alpha = 1.0$.

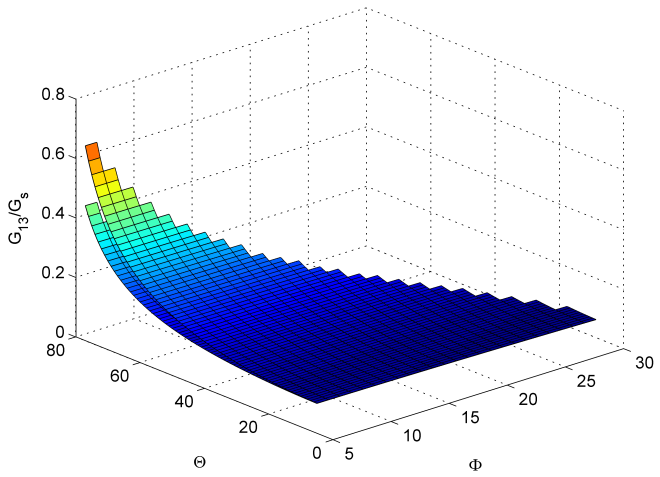


Figure 17 Theoretical upper bound and numerical lower bound of the non-dimensional transverse shear modulus vs. $\varphi$ and $\theta$ for $\beta = 0.1, \gamma = 1, \alpha = 2.0$.

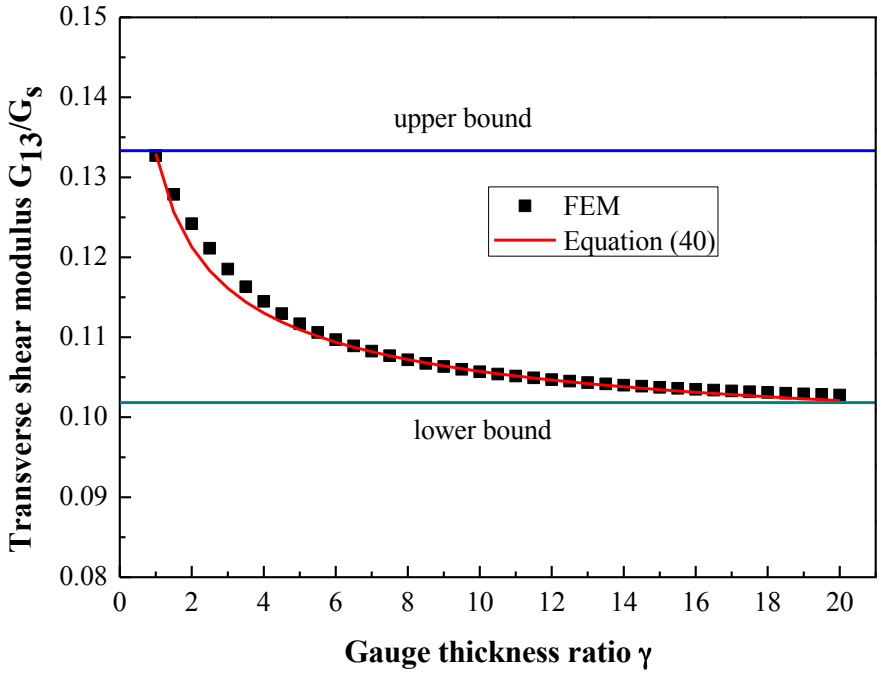


Figure 18 Non-dimensional transverse shear modulus $G_{13}/G_S$ vs. γ for $\alpha = 1, \varphi = \theta = 30°, \beta = 0.1$.

## 6 CONCLUSIONS

In this work, a novel zero Poisson's ratio honeycomb structure has been designed, modeled and evaluated from an analytical and numerical point of view. The investigation focused on the effects of the unit cell geometrical configurations to the in-plane properties (Young's modulus, in-plane shear modulus, and Poisson's ratio) and out-of-plane properties (transverse shear modulus). The theoretical and numerical models show a general excellent agreement. The novel zero Poisson's ratio honeycomb shows the possibility of performing two dimensional deformations with tailored stiffness that could be used to design zero Poisson's ratio cellular honeycomb structures for planar morphing applications.


### Acknowledgements

The support of the FP7-AAT.2012.6.3-1-341509 MORPHELLE and the National Natural Science Foundation of China (Grant No.11225211, 11272106) are gratefully acknowledged. Xiaobo Gong and Jian Huang would also like to thank British Council and Chinese Scholarship Council (CSC) for the funding of his research work through University of Bristol.

**REFERENCES**

[1] Barbarino S, Bilgen O, Ajaj RM, Friswell MI, Inman DJ. A review of morphing aircraft. Journal of Intelligent Material Systems and Structures. 2011;22:823-77.
[2] Sofla A, Meguid S, Tan K, Yeo W. Shape morphing of aircraft wing: Status and challenges. Materials & Design. 2010;31:1284-92.
[3] Thill C, Etches J, Bond I, Potter K, Weaver P. Morphing skins. The Aeronautical Journal. 2008;112:117-39.
[4] Kikuta MT. Mechanical properties of candidate materials for morphing wings: Virginia Polytechnic Institute and State University, 2003.
[5] Olympio KR, Gandhi F. Flexible skins for morphing aircraft using cellular honeycomb cores. Journal of Intelligent Material Systems and Structures. 2009.
[6] Olympio KR, Gandhi F. Zero-Nu Cellular Honeycomb Flexible Skins for One-Dimensional Wing Morphing. 48th Structures, Structural Dynamics, and Materials Conference2007. p. 23-6.
[7] Gibson LJ, Ashby MF. Cellular solids: structure and properties: Cambridge university press, 1997.
[8] Masters I, Evans K. Models for the elastic deformation of honeycombs. Composite Structures. 1996;35:403-22.
[9] Bitzer T. Honeycomb technology: materials, design, manufacturing, applications and testing: Springer Science & Business Media, 1997.
[10] Gibson L, Ashby M, Schajer G, Robertson C. The mechanics of two-dimensional cellular materials. Proceedings of the Royal Society of London A: Mathematical, Physical and Engineering Sciences: The Royal Society; 1982. p. 25-42.
[11] Grediac M. A finite element study of the transverse shear in honeycomb cores. International Journal of Solids and Structures. 1993;30:1777-88.
[12] El-Sayed FA, Jones R, Burgess I. A theoretical approach to the deformation of honeycomb based composite materials. Composites. 1979;10:209-14.
[13] Almgren RF. An isotropic three-dimensional structure with Poisson's ratio--1. Journal of Elasticity. 1985;15:427-30.
[14] Scarpa F, Burriesci G, Smith F, Chambers B. Mechanical and electromagnetic behaviour of auxetic honeycomb structures. Aeronautical Journal. 2003;107:175.
[15] Scarpa F, Tomlinson G. Theoretical characteristics of the vibration of sandwich plates with in-plane negative Poisson's ratio values. Journal of Sound and Vibration. 2000;230:45-67.
[16] Lira C, Innocenti P, Scarpa F. Transverse elastic shear of auxetic multi re-entrant honeycombs. Composite Structures. 2009;90:314-22.
[17] Murray GJ, Gandhi F. Auxetic honeycombs with lossy polymeric infills for high damping structural materials. Journal of Intelligent Material Systems and Structures. 2013:1045389X13480569.
[18] Chen Y, Scarpa F, Liu Y, Leng J. Elasticity of anti-tetrachiral anisotropic lattices. International Journal of Solids and Structures. 2013;50:996-1004.
[19] Bornengo D, Scarpa F, Remillat C. Evaluation of hexagonal chiral structure for morphing airfoil concept. Proceedings of the Institution of Mechanical Engineers, Part G: Journal of Aerospace Engineering. 2005;219:185-92.
[20] Prall D, Lakes RS. Properties of a chiral honeycomb with a poisson's ratio of — 1. International Journal of Mechanical Sciences. 1997;39:305-14.
[21] Lorato A, Innocenti P, Scarpa F, Alderson A, Alderson K, Zied K, et al. The transverse elastic properties of chiral honeycombs. Composites Science and Technology. 2010;70:1057-63.

[22] Theocaris P, Stavroulakis G, Panagiotopoulos P. Negative Poisson's ratios in composites with star-shaped inclusions: a numerical homogenization approach. Archive of Applied Mechanics. 1997;67:274-86.
[23] Alderson A, Alderson K. Auxetic materials. Proceedings of the Institution of Mechanical Engineers, Part G: Journal of Aerospace Engineering. 2007;221:565-75.
[24] Larsen UD, Signund O, Bouwsta S. Design and fabrication of compliant micromechanisms and structures with negative Poisson's ratio. Microelectromechanical Systems, Journal of. 1997;6:99-106.
[25] Olympio KR, Gandhi F. Zero Poisson's ratio cellular honeycombs for flex skins undergoing one-dimensional morphing. Journal of Intelligent Material Systems and Structures. 2010;21:1737-53.
[26] Attard D, Grima JN. Modelling of hexagonal honeycombs exhibiting zero Poisson's ratio. physica status solidi (b). 2011;248:52-9.
[27] Lira C, Scarpa F, Olszewska M, Celuch M. The SILICOMB cellular structure: Mechanical and dielectric properties. physica status solidi (b). 2009;246:2055-62.
[28] Virk K, Monti A, Trehard T, Marsh M, Hazra K, Boba K, et al. SILICOMB PEEK Kirigami cellular structures: mechanical response and energy dissipation through zero and negative stiffness. Smart Materials and Structures. 2013;22:084014.
[29] Bezazi A, Scarpa F, Remillat C. A novel centresymmetric honeycomb composite structure. Composite Structures. 2005;71:356-64.
[30] Bubert EA, Woods BK, Lee K, Kothera CS, Wereley NM. Design and fabrication of a passive 1D morphing aircraft skin. Journal of Intelligent Material Systems and Structures. 2010;21:1699-717.
[31] Vocke RD, Kothera CS, Woods BK, Wereley NM. Development and testing of a span-extending morphing wing. Journal of Intelligent Material Systems and Structures. 2011:1045389X11411121.
[32] Liu W, Zhu H, Zhou S, Bai Y, Wang Y, Zhao C. In-plane corrugated cosine honeycomb for 1D morphing skin and its application on variable camber wing. Chinese Journal of Aeronautics. 2013;26:935-42.
[33] Young WC, Budynas RG. Roark's formulas for stress and strain: McGraw-Hill New York, 2002.
[34] Lira C, Scarpa F, Tai Y, Yates J. Transverse shear modulus of SILICOMB cellular structures. Composites Science and Technology. 2011;71:1236-41.
[35] Scarpa F, Tomlin P. On the transverse shear modulus of negative Poisson's ratio honeycomb structures. Fatigue & Fracture of Engineering Materials & Structures. 2000;23:717-20.
[36] Kelsey S, Gellatly R, Clark B. The shear modulus of foil honeycomb cores: A theoretical and experimental investigation on cores used in sandwich construction. Aircraft Engineering and Aerospace Technology. 1958;30:294-302.